

# Experimental and Numerical Investigation of Active Control of Inlet Ducts

John C. Vaccaro, Onkar Sahni, Joseph Olles, Kenneth E. Jansen, and Michael Amitay<sup>1</sup>

Mechanical, Aerospace and Nuclear Engineering Department,  
Rensselaer Polytechnic Institute, Troy, NY 12180, USA

<sup>1</sup>Corresponding Author; E-mail: amitam@rpi.edu

The effect of steady and unsteady control jets on the performance of a very aggressive (length to exit diameter ratio,  $L/D$ , of 1.5) inlet duct was investigated. Experiments were performed for a range of inlet Mach numbers from 0.2 to 0.45 and compared with numerical simulations for the baseline flow case at an inlet Mach number of 0.45. A brand new facility was designed and built to enable various actuation methodologies as well as multiple measurement techniques. In the present work, a pair of control jets was placed in streamwise locations where flow was expected to separate. Steady and unsteady static pressure measurements, along the upper and lower walls of the duct, were performed for various combinations of actuation. The parameters that were tested include the control jets momentum coefficient, the blowing ratio, the actuation frequency, as well as different combinations of jets. It was shown that using mass flux ratio as a criterion to define flow control is inappropriate, and one needs to provide both the momentum coefficient and the blowing ratio to quantify the flow control performance. In addition, steady and unsteady total pressure measurements were conducted at the Aerodynamic Interface Plane (AIP) to obtain the distribution of the pressure recovery and surface pressure. Furthermore, the interaction of the control jets with the main flow was explored using Particle Image Velocimetry. Flow control was found to be more effective at the lower Mach number where the blowing ratio was higher (for the same mass flux ratio). The data suggest that unsteady actuation is more effective (compared to steady blowing) and more efficient (requires less input pressure). As expected, using 2-D actuators to affect a highly 3-D flow field is not optimal, and as such a spanwise varying actuation should be implemented in future work.

The numerical simulations employed a stabilized finite element method to perform turbulence computations (Jansen, 1999) using two variants of the Spalart-Allmaras (S-A) model; the original one-equation S-A model (Spalart et. al., 1992) in an unsteady Reynolds-averaged Navier-Stokes simulation (URANSS) and a hybrid S-A model (Spalart et. al., 1997) in a detached eddy simulation (DES). While the inclusion of unsteadiness in URANSS is a step in the right direction, the basic deficiencies of RANSS for adverse pressure gradient, separated flows lead to poor prediction for a flow this complex. On the other hand, DES results are in good agreement with the experimental measurements. Specifically, URANSS model predicts two large, stable vortices at the lower corners that pull the flow down at the centerline and thus, leads to higher pressure values and under predicts the flow separation on the centerline.

## 1. INTRODUCTION

The inlet to an aircraft propulsion system is typically designed to supply flow to the compressor with minimal pressure loss, distortion, or unsteadiness. Otherwise, the overall system performance will be reduced, which can result in stall or surge of the compressor and a catastrophic failure of the engine. While the inlet length that is required to avoid separation and its associated losses may not be a significant design driver for some aircraft, other applications require a short inlet length due to integration and packaging constraints, and others because the inlet length can drive the size of the overall aircraft (i.e., production and operating costs). Therefore, technologies such as passive or active flow control that can enable shorter inlets could have significant overall system benefits.

Current aircraft designs typically consider the compressor and inlet as separate sub-systems, where the connection between them is given as a pressure recovery and distortion specification that must be met at the Aerodynamic Interface Plane (AIP). As is expected of an engine intake, the flow must be decelerated whilst achieving as uniform a flow as possible at the compressor face with minimum

stagnation pressure loss. Short inlets will have high degrees of centerline curvature. Due to centerline curvature, there are cross-stream pressure gradients resulting in migration of boundary layer fluid in the direction of the pressure gradient giving rise to secondary flows. Within the boundary layer this imparts cross-flow velocities creating non-uniform total pressure profiles. In addition, there is a streamwise pressure gradient resulting from increasing cross-sectional area. The combined effect results in increased total pressure non-uniformity (i.e., distortion) and total pressure loss at the inlet exit. The intake must not only deliver air to the engine with minimum total pressure loss but also flow at the compressor face with minimum distortion.

The application of flow control devices for inlets has been investigated since the late 1940s using vortex generator vanes to re-energize the boundary layer to prevent flow separation. In the early 1970s it was demonstrated that vortex generators can result in restructuring of the development of the secondary flow and thus improve engine face distortion. This suggests that in order to effectively improve the inlet performance, separation control is not sufficient and a global manipulation of the secondary inlet flow must be implemented. This approach would require inlet flow control designs to address the three dimensionality of the flow field. While there has been significant research on inlet flow control, there has been very little research on closed-loop active inlet control, in general, and especially in multidisciplinary research with actuation systems that incorporate unsteady components (e.g., Power Resonance Tubes, unsteady blowing, and synthetic jets). The present manuscript presents an ongoing research on active flow control of an inlet with  $L/D = 1.5$ . This is a very aggressive configuration, which was chosen in order to test the limit of active flow control.

Over the years, several passive and active flow control techniques have been developed. Passive techniques are characterized by no energy input into the fluid, whereas active techniques are characterized by a net energy input into the flow, by means of moving parts (Neuberger and Wygnanski, 1987), acoustic excitation (Ahuja and Burrin, 1984), fluidic injection or synthetic jets (Amitay et al., 2001). The main passive control technique is the Vortex Generator (VG) technique. VGs are small surfaces of various shapes (rectangular, triangular, etc.) that are extruded from the surface and are used to generate streamwise vortices to enhance mixing. This technique was largely studied (e.g., Allan et al., 2002), and was shown to be quite efficient at delaying or even suppressing separation mainly on airfoils, but also in air inlets. The main drawback of using vortex generators is the parasitic drag they induce.

The main active control techniques are steady or unsteady blowing or suction. Vortex Generator Jets (VGJ), for example, were developed to minimize the VGs parasitic drag. They are very similar to VGs, but streamwise vortices are generated by a pulsating jet perpendicular to the wall. Suction and blowing can also simply be applied through a slot, usually tangential to the wall in order to benefit from the Coanda effect (Panitz and Wasan, 1972). Active flow control techniques are typically used to exploit the combined narrow-band receptivity of the separating shear layer and the upstream boundary layer to external actuation (e.g., Ho & Huerre, 1984). Oster & Wygnanski (1982) showed that the actuation can affect the global flow field by modifying the evolution and interactions of the large-scale vortical structures. These modifications can lead to a Coanda-like deflection of the separating shear layer towards the surface (e.g., Seifert et al., 1996) such that the layer vortices are advected downstream in close proximity to the surface.

This approach has been implemented, with varying degrees of success and different actuation means, to restore aerodynamic performance of stalled airfoils and flaps. In particular, Seifert et al. (1993) and Wygnanski (2000) argued that the actuation is most effective when its period scales with the advection time through the length of the flow domain downstream of separation as measured by the reduced frequency,  $F^+$ . Therefore, when the separation domain scales with the characteristic length of an aerodynamic body, the (dimensionless) actuation frequency can couple to, and even drive the shedding frequency in the near wake. The possibility of coupling between (nominally) time-periodic shedding of coherent vortices and the separated shear layer in the absence of actuation is intriguing because such feedback between the near wake instabilities and the separating shear layer is even more pronounced in the presence of actuation thereby amplifying the unsteady component of the global aerodynamic forces. The approach of coupling the actuation frequency to instabilities that are inherent to separated flows relies explicitly on the narrow-band receptivity of the separating shear layer to a control input. Therefore, it is effective within a limited spatial domain immediately upstream of separation.

Another approach to control the flow is based on fluidic modification of the apparent aerodynamic shape of lifting surfaces using integrated synthetic jet actuators (Glezer and Amitay, 2002) that are

driven at high frequencies (i.e., much larger than the characteristic frequencies of the flow; a discussion on this approach was presented by Amitay & Glezer, 1999 and 2002). Thus, this approach does not necessarily rely on coupling to global flow instability and therefore can be applied over a broader range of flow conditions (e.g., Amitay et al., 2001 and Amitay & Glezer, 2002). This approach was implemented by Amitay et al. (2002), where active control of separation in a  $L/D = 3$  duct flow was achieved using an array of synthetic jets. Actuation led to complete flow attachment up to  $M \approx 0.2$  and to partial reattachment up to  $M \approx 0.3$ .

In the last two decades different control techniques have been experimentally implemented on inlet ducts: vortex generators, steady blowing, unsteady blowing, and more. For example: micro-vane type vortex generators and vortex generator jets were implemented by Lockheed Martin and NASA on a very aggressively designed inlet at a flight Mach number of 0.6 (Hamstra et al., 2000). In their study, an array of 36-micro vanes was shown to have beneficial effect on pressure recovery, with somewhat mitigated results with the VGJ. An example for an active control, Luers (2003) conducted a parametric study on an aggressive inlet using pulsating injection at the separation line at flight Mach number of  $M = 0.6$  with very promising results.

## 2. EXPERIMENTAL SETUP

A brand new inlet duct facility was designed and built at Rensselaer Polytechnic Institute (RPI). The facility can achieve Mach numbers of up to 0.5 (or mass flow rates of up to  $\sim 2.3$  kg/s). The duct has an  $L/D$  ratio of 1.5 with a rectangular cross-section (114.3 mm wide x 88.9 mm high) at the inlet and a square cross section (114.3 mm wide x 114.3 mm high) at the outlet from the duct. Figure 1 presents the design layout of the new facility, which includes a blower, a diffuser, a settling chamber, a contraction, an inlet duct, and a downstream diffuser. The facility enables testing of various active flow control actuators (Figure 2) to reattach the separated flow and to provide as uniform a total pressure field as possible at the AIP.

The blower used is a Cincinnati Fan model HP-12G29, which has the capacity to overcome 65 in of static water pressure and produce a volumetric flow rate of up to 6000 ft<sup>3</sup>/min. It is run by a 100 HP motor and controlled by a Variable Frequency Drive (VFD). The air then enters a diffuser section, followed by a settling chamber. The settling chamber incorporates a honeycomb, and a screen. The flow transitions from the settling chamber to the test section through a contraction section. This section has a standard fifth order polynomial curvature and is made from 3.175mm stainless steel reinforced by 6.35mm thick ribs. The contraction starts from the 1.22m x 1.22m section of the settling chamber and reduces to the 88.9mm x 114.3mm area of the inlet test section. Following the contraction section is a constant cross-section area section having a length of 105.1mm. At this section, the Mach number and mass flow rate are measured. Measurements acquired at this section (50.8mm downstream of the end of the contraction) include a static pressure ring (using four static pressure measurements centered on each wall at one particular axial location). Also at this same location, the total pressure is measured using a Kiel total pressure probe. The inlet Mach number is determined using the static pressure measurements, along with the total pressure, through:

$$M_{in} = \sqrt{\left[ \left( \frac{P_0}{P} \right)^{\frac{\gamma-1}{\gamma}} - 1 \right] \left( \frac{2}{\gamma-1} \right)} \quad (1)$$

Since it is undesirable to have the probe in the flow during testing, the static pressure ring and the total pressure in the settling chamber were calibrated against the Kiel probe prior to testing and were used to monitor the Mach number. The mass flow through the test section is determined from the isentropic flow equations along with the average Mach number (note that the stagnation conditions are determined from the ideal gas law).

As mentioned above, the inlet of the duct is of rectangular cross-section while the cross-sectional area at the outlet of the duct is a square. The walls of the test section are made of 19.05mm optical-grade Lexan, which was chosen for its optical qualities to enable Particle Image Velocimetry (PIV) measurements.

Following the inlet duct is a diffuser (with a 3 deg diffusion angle) that was used to diffuse the flow and reduce its speed before it left the facility (and discharged into the room), as well as to lower the throat static pressure and reduce the total pressure head.

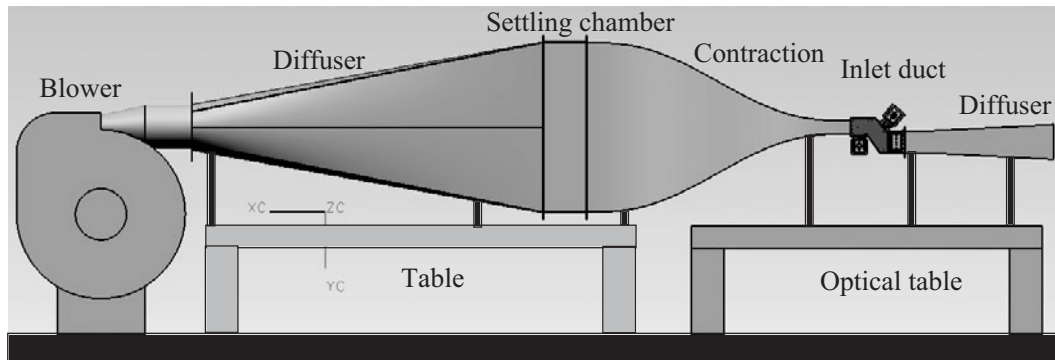


Figure 1. Design layout of the inlet duct facility.

At two corners of the transition section, specially designed actuators were placed to control the separation (see Figure 2). The actuators that were used can provide steady or unsteady blowing using rotary-valve-based actuators (Figure 3). The actuator uses a compressed air source which feeds the actuator with the desired air pressures and flow rates. In line are a valve used to regulate the mass flow, a flow meter, a pressure transducer and a thermocouple (to correct the flow meter reading, as well as to calculate the local density needed to evaluate the mass flux), the rotary valve body, the resonator and the injector itself, which brings the flow up to the inlet duct wall (the air delivery system for the flow control actuators is shown in Figure 2). The rotary valve produces unsteady flow, and it consists of the valve body encasing a cylindrical rotor driven by an electric motor. The center of the rotor itself is empty, so that the flow fills the interior of the rotor and passes through 10 slots that are machined in the rotor side walls. As the rotor spins in the valve body, the rotor slots align periodically with a slot machined in the valve body, which connects the exit of the valve body to the resonator. The result is an oscillatory pressure in the resonator cavity. By adjusting the input voltage to the DC motor its frequency is varied and thus the frequency of the fluctuating pressure can be adjusted. The resonator is a rectangular cavity with dimensions chosen such that it resonates at the desired frequency range (in the present experiments, frequencies of 350Hz, 800Hz, and 1200Hz were tested). The cavity then feeds the

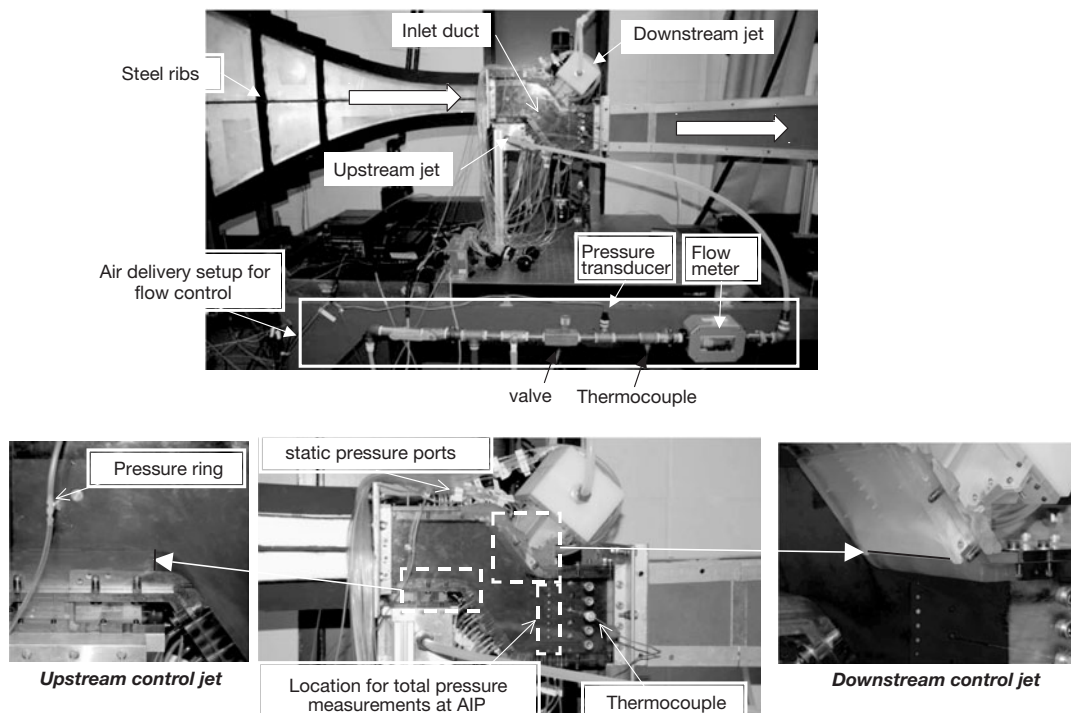


Figure 2. Photos of the experimental facility.

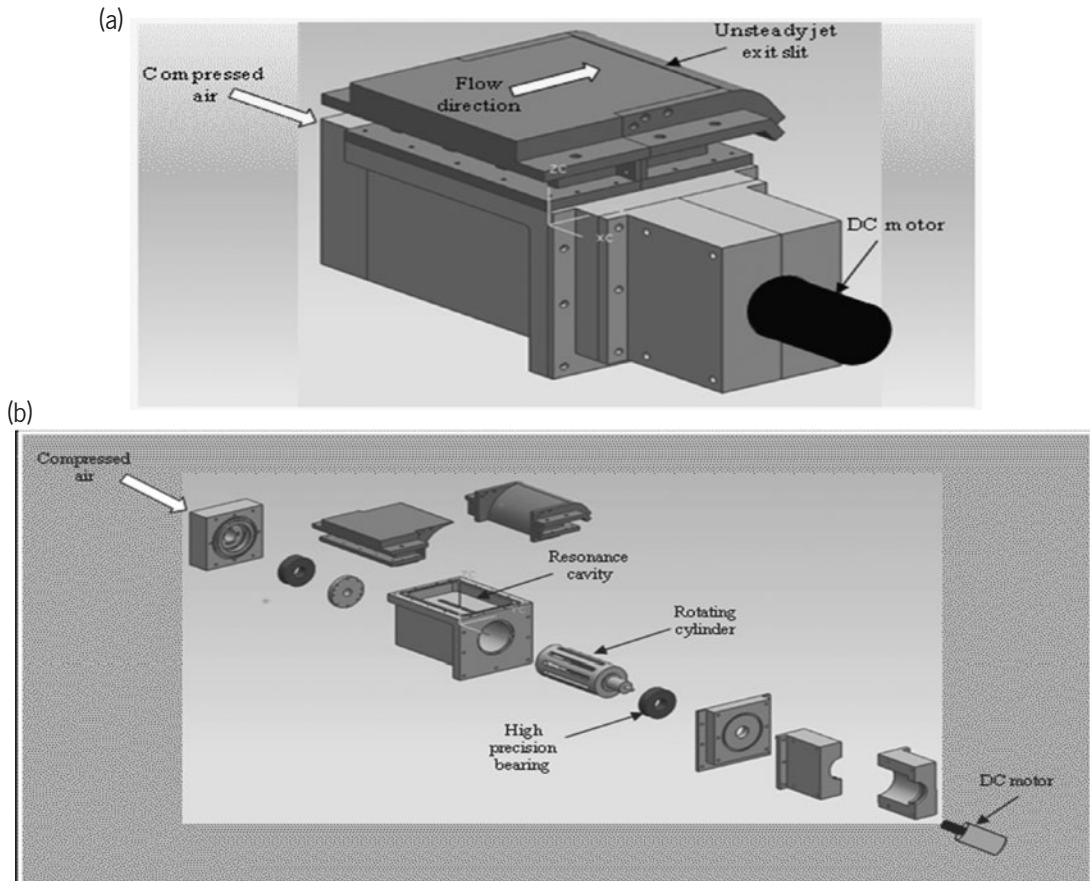


Figure 3. CAD drawing of the rotary valve actuator; assembly (a), and exploded view (b)

injector block, whose role is to reduce the flow path area so that the fluid velocity reaches its maximum at the injector exit slot, and to redirect the flow so that it is delivered tangentially to the inlet wall through a rectangular slit. The rectangular slit is located just upstream of the turn and it is 101.6mm in length and its width is either 0.5mm or 1mm. The velocity distribution along the jet slit is uniform (within 1%) for 80% of its length (not shown).

The facility incorporates 72 static pressure ports along the duct centerline and on both sides of centerline (44.45mm off-centerline), which were measured using a pressure scanner. Steady total pressure measurements at the AIP were conducted using 3 Kiel probes to create a grid of 81 points, as shown in Figure 4. Due to symmetry, only 45 data points were acquired for each case (marked by the

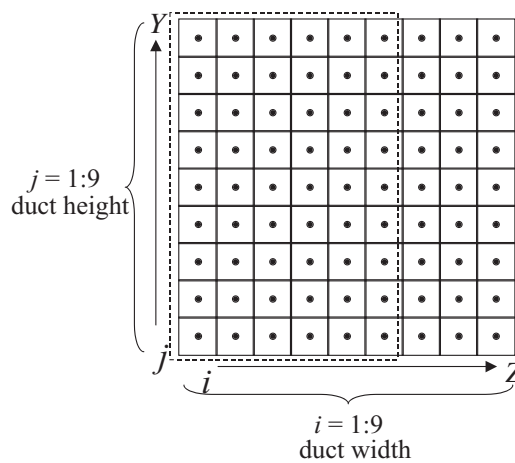


Figure 4. AIP measurement grid.

dashed line in Figure 4). Note that in Section 4.3 only 25 data points were used to calculate the pressure recovery at the AIP (discussion on that is presented in that section).

The effect of flow control on the unsteady pressure along the lower wall and at the AIP was also investigated. Six Kulite dynamic pressure sensors (full scale of 25psia and accuracy of  $\pm 0.1\%$  of full scale) were placed in various locations in the duct (Figure 5) and a seventh sensor was placed in the resonance cavity of the actuator. Kulites 1, 2, and 3 were located along the centerline at  $x/D_{AIP} = 0.47$ , 0.83, and 1.12, respectively, and Kulites 4 and 5 are at the same streamwise location as Kulite 1 but off the centerline at  $z/D_{AIP} = 0.11$  and 0.89, respectively. The sixth Kulite was located at the AIP ( $y/D_{AIP} = 0.306$  and  $z/D_{AIP} = 0.5$ ). Both instantaneous and phase averaged data were collected.

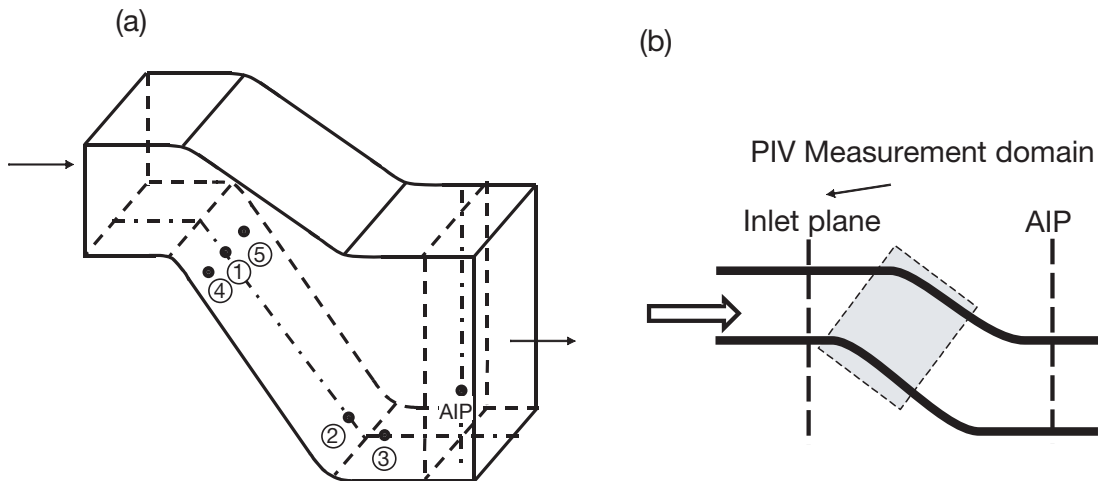


Figure 5. Schematics of (a) dynamic pressure sensors locations, and (b) PIV measurement domain.

The interaction of the control jets with the cross-stream was captured and investigated through the use of Particle Image Velocimetry (PIV). Two dimensional velocity vector fields, in the streamwise direction, were collected in three spanwise locations, focusing on the location near the upstream jet to explore the interaction between the jet and the main flow and its ability to reattach the flow (Figure 5b). The PIV system used is a commercial LaVision System of hardware and software including two 120 mJ Nd:YAG lasers and a 1376 x 1040 pixel resolution thermo-electrically cooled 12-bit CCD camera. A 20 mm cylindrical lens was used to create the light sheet and a focal lens (with a focal length range of 500mm to 1500mm) was used to focus the sheet at the measurement domain (the thickness of the light sheet at the center of the measurement domain was about 1mm). The laser light sheet was then aligned with the area of interest using a computer-controlled three axis traversing system mounted on an optical table. Flow was seeded with  $O(1\mu\text{m})$  smoke particles, generated by a theatrical fog machine that was added to the flow through the blower. The flow field was imaged using the CCD Camera mounted on its own independently controlled three axis traverse. Measurements were acquired at 3 spanwise planes ( $z/D_{AIP} = 0.238, 0.367, \text{ and } 0.5$ ).

The streamwise velocity components ( $U, V$ ) were computed from the cross-correlation of pairs of successive images with 50% overlap between the interrogation domains. The images were processed using an advanced multi-pass method where the initial and final correlation passes were  $64 \times 64$  pixels and  $32 \times 32$  pixels, respectively. 200 image pairs were acquired. The camera was mounted at a perpendicular distance of approximately 1m to the laser light, such that the distance between pixels is  $\sim 20\text{mm}$ . The maximum velocity ( $\sim 250\text{m/s}$ ) corresponds to an average displacement of approximately  $\sim 8$  pixels with an approximate error of  $\pm 0.1$  pixels, which corresponds to a maximum error of  $\pm 1.25\%$  of the free-stream velocity ( $\pm 3.1\text{m/s}$ ).

### 3. NUMERICAL SIMULATION METHODOLOGY

High Reynolds number, adverse pressure gradient separated flows, like the one considered here, have for a long time posed a great challenge to numerical simulation. The Reynolds number is far too high for direct numerical simulation (DNS). At the other extreme, steady Reynolds-averaged Navier-Stokes simulation (RANSS) have struggled with adverse pressure gradient separation. While one can attempt

to consider large eddy simulation (LES) in a thin extrusion of a centerline cross section, the experimental results show the futility of such an approach due to the inherently three-dimensional flow created in such an inlet duct with high curvature and cross-section of nearly one aspect-ratio. Therefore, two types of turbulence simulations are considered; unsteady Reynolds-averaged Navier-Stokes simulation (URANSS) using the original one equation S-A model (Spalart et. al. 1992) and detached eddy simulation (DES) based on a hybrid S-A model (Spalart et. al. 1997).

In this study the computational domain incorporates a contraction section prior to the inlet duct to match the experimental setup as shown in Figure 1 and also includes a straight section after the exit of the duct. The duct inlet Mach number of 0.45 is considered which is attained by prescribing a plug velocity profile and constant temperature at the entry of the contraction. A no-slip boundary condition is imposed at the walls that are assumed to be isothermal and static pressure is specified at the exit of the domain. Flow computations are performed using the Streamline Upwind Petrov-Galerkin (SUPG) stabilized finite element method (Jansen, 1999), which has been proven stable and higher order accurate (converging at the optimal rate for a given function space).

To develop a numerical method, the variables are expressed in terms of basis functions (typically piecewise polynomials; all calculations herein were performed with linear basis). The integrals in the discretized equations are then evaluated numerically using Gauss quadrature resulting in a system of non-linear ordinary differential equations. The system of non-linear ordinary differential equations obtained is integrated in time via a second-order generalized-alpha time integrator (Jansen et al., 1999) resulting in a non-linear system of algebraic equations. The non-linear system of algebraic equations obtained is in turn linearized with Newton's method which yields a linear algebraic system of equations. The GMRES method (Saad et. al., 1986), with sparse storage and a block-diagonal preconditioner, is used to solve the linear system of equations. Note that the Reynolds-averaged Navier-Stokes equations along with the S-A eddy viscosity equation are solved in a staggered form to achieve non-linear convergence of the combined equations at every time step.

Furthermore, adaptive meshing techniques developed for unstructured grids including boundary layer elements (Sahni et. al., 2008) are utilized to make such flow simulations practically feasible and efficient. To carry out the adaptive mesh-based flow simulations we perform the flow computations and evaluate the quality of the computed solution on the current mesh to determine its suitability. These error indicators can also be combined with flow feature identification to concentrate early adaptivity on regions known to be important. For example, in this study, we use pressure loss to determine the presence of flow features such as separation and secondary flows, and to improve the mesh resolution locally in these regions. The adaptive techniques used in this study are capable of maintaining the layered structure present in such meshes near the walls due to the presence of boundary layer elements (Sahni et. al., 2007) that are critical for viscous flow simulations.

The initial, unstructured mesh containing boundary layer elements near the walls is shown in Figure 6a. Such a mesh is commonly referred to as boundary layer mesh or semi-structured mesh (Pirzadeh et. al., 1994, Garimela et. al., 2000), and maintains desirable attributes for high-Reynolds number flow simulations due to use of high-aspect ratio, orthogonal, layered and graded elements near the walls. Care is taken to produce elements of acceptable shape at turns and corners within the domain; and also to ensure a smooth transition between the layered part and the interior tetrahedral part of the mesh as can be seen in Figure 6a from the interior mesh faces near the fillet at the lower flow control slot. Moreover, use of completely unstructured tetrahedral elements elsewhere in the interior of the domain allows for significant but smooth (graded) variation of local mesh resolution making simulations practically feasible.

In the current mesh, for example, the length of mesh-edges in the contraction section is about  $h_{contraction} = D_{AIP}/2$ , whereas mesh-edges near the flow control slots are of length  $h_{slot} = D_{AIP}/2000$  ( $=0.05715\text{mm}$ ); resulting in a change of local mesh resolution by three orders of magnitude. Also note that the length of mesh-edges at the central core of the inlet duct is  $h_{throat} = D_{AIP}/20$  (including portions around the vertical planes passing through the flow control slots), leading to variation of mesh resolution by a factor of 100 as compared to mesh-edges near the flow control slots. This initial distribution of mesh sizes is based on preliminary insight but it is important to point out that the precise resolution needs of the flow in such a complicated geometry cannot be fully defined prior to the simulation. Therefore, such initial meshes are constructed to allow the use of mesh adaptivity for subsequent more resolved simulations, where the mesh resolution can be changed (locally) based on the quality of the computed solution features. Use of such techniques in turn allows for efficient simulations of real-life problems by focusing mesh resolution in regions of interest.

Figure 6b shows the initial and adapted boundary layer meshes used in the current study. The two meshes contain about 2.5 and 4 million points and are referred as  $M_{coarse}$  and  $M_{fine}$ , respectively. The adapted mesh contains finer resolution only in specific portions after both of the turns in the inlet duct. This adaptivity effectively provides a uniform refinement of the regions with flow separation and secondary flows (that are shown in the results section). Within the layered elements, only the in-plane resolution of boundary layer elements was adapted while the normal-direction resolution thickness of the layered elements was held fixed at  $y^+$  values that maintained the first grid points off the walls at order 1 or lower.

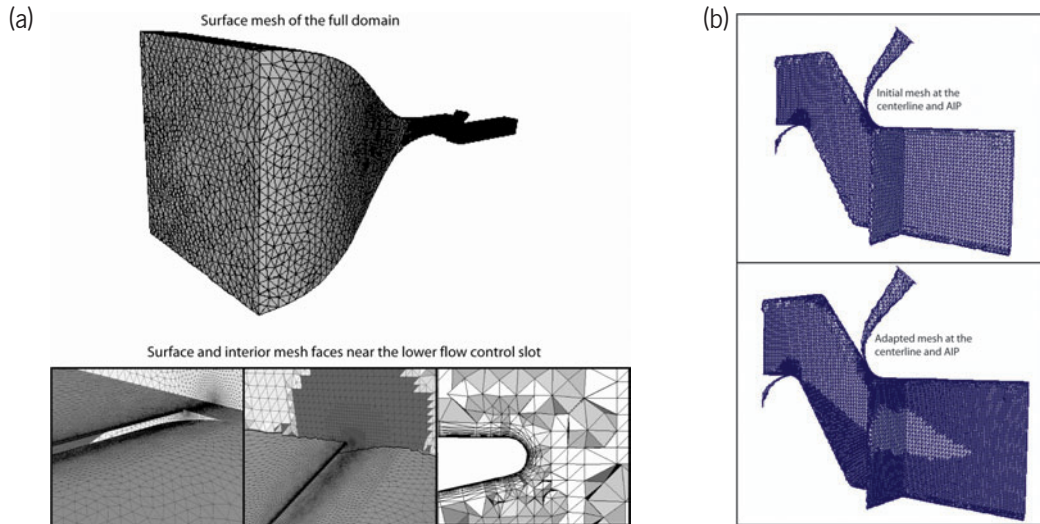


Figure 6. (a) Mesh of the full computational domain including contraction, serpentine inlet duct and straight section with magnified views of surface mesh and interior mesh faces near the lower flow control slot, and (b) Initial and adapted meshes (near the inlet duct) at the AIP plane and the vertical center-plane.

The numerical results presented here are those obtained from three different simulations of the baseline flow (no flow control) configuration; (a) URANSS on initial (coarser) mesh  $M_{coarse}$ , (b) URANSS on adapted (finer) mesh  $M_{fine}$  and (c) DES on the adapted mesh  $M_{fine}$ . URANSS results on both the meshes are included to demonstrate that the URANSS using the original one-equation S-A model provide negligible improvements with grid refinements in the regions of interest and therefore, indicating that URANSS fails to predict the key aspects of this complex flow with adverse pressure gradient and flow separation. Note that the simulations including flow control cases are not included in this paper though work is underway to simulate those cases (similar to the ones considered in the experiments). Given the massive computational resources required for these simulations, the numerical results presented here are focused on establishing the required modeling and resolution needed in the baseline case before embarking on a study of the flow control cases presented in the experiment section.

The time step size on the adapted (finer) mesh was fixed to a value of  $6.125 \mu\text{sec}$ , leading to 180 steps per inlet-duct flight-time based on the centerline velocity at the entry of the duct and the length of the inlet duct (entry to AIP). The results presented on the adapted mesh compute average quantities using 200 samples equally distributed over 10,000 time steps or about 56 flight-times. Average quantities using 1,000 samples over the same time interval produced similar results with insignificant differences. Comparing samples in the two halves of this physical time interval also led to insignificant differences. In terms of computational resources, simulations on the refined mesh were performed using 1,024 processors at a rate of about one flight-time per hour (computations in this study were carried out on the Ranger system at the Texas Advanced Computing Center and the Opteron Blade Cluster at the Computational Center for Nanotechnology Innovations). Note that the current analysis code (PHASTA) has been shown to scale at  $O(10^4)$  processors (Shephard et. al., 2007 Sahni et al., 2009).

#### 4. RESULTS

The experiments were conducted for three Mach numbers of 0.2, 0.325 and 0.45 for the baseline case (i.e., no flow control) and various combinations of active flow control. The flow control was

implemented using two control jets; one was located at the first turn on the lower surface, and one on the second turn on the upper surface (upstream and downstream control jets, respectively, Figure 2). The forcing level is determined using two parameters: the control jet momentum coefficient ( $C_\mu$ , which is the ratio of the momentum of the control jet to the momentum of the flow at the inlet plane), and the blowing ratio,  $C_b$ , the ratio of the control jet Mach number to the inlet Mach number) defined as:

$$C_\mu = \frac{\rho_j U_j^2 b h}{\rho_{in} U_{in}^2 B H} \quad (2)$$

where  $\rho_j$  and  $\rho_{in}$  are the densities of the control jet at its exit plane and the main flow in the duct measured at the inlet plane, respectively.  $U_j$  and  $U_{in}$  are the control jet exit velocity and the main flow velocity at the inlet plane, respectively, while  $b$ ,  $h$  and  $B$ ,  $H$  are the dimensions of the control jet slit and the duct inlet, respectively.

$$C_b = \frac{M_j}{M_{in}} \quad (3)$$

The level of forcing is determined by many researchers as a percentage ratio of control jets mass flux to the main flow inlet mass flux (e.g., Rabe et al., 2006; Tournier et al, 2006; Debiasi et al, 2008) measured at the duct inlet) as:

$$\hat{m} = 100 \cdot \frac{\dot{m}_{actuators}}{\dot{m}_{inlet}} \quad (4)$$

where  $\dot{m}_{actuators}$  is the mass flux of the control jets, and  $\dot{m}_{inlet}$  is the mass flux of the main flow. However, as is shown in the present paper,  $\hat{m}$  is an inappropriate parameter to describe the flow control strength.

#### 4.1 Static Pressure Distributions – Steady Control Jets

In this section data were acquired for  $M = 0.2, 0.325$  and  $0.45$  for the baseline case and actuated cases using steady blowing (the slit width is 1mm). Figure 7 presents the streamwise distributions of the pressure coefficient  $C_p$ ,  $C_p = (p - p_{s\_in})/(p_o - p_{s\_in})$ , along the duct centerline on the lower surface (Figure 7a) and upper surface (Figure 7b) at  $M = 0.2$  (where  $p$  is the local static pressure,  $p_{s\_in}$  is the incoming static pressure measured by the static ring, and  $p_o$  is the stagnation pressure). Four cases are presented: the baseline case (i.e., no flow control) and three control cases (upstream jet only, downstream jet only, and both jets together) where the momentum coefficient for each forced case is  $C_\mu = 0.0316$  ( $\hat{m} = 3\%$ ). Without flow control (diamond symbols), the flow is separated downstream of the first turn on the lower surface (Figure 7a) and reattaches just downstream of the second turn (at  $x/D_{AIP} = 1.2$ ). Here,  $D_{AIP}$  is the width of the duct at the AIP ( $D_{AIP} = 114.3\text{mm}$ ), which was kept constant along the duct. When the upstream jet is activated (star symbols) the extent of the separation region along the lower surface is reduced and the static pressure recovery is significantly increased. When the downstream jet is activated (triangle symbols), there is a slight increase in the pressure coefficient throughout the measurement domain. As expected, the effect of the upstream jet on the pressure distribution along the lower wall is much more pronounced than the downstream jet. When both control jets are activated (circle symbols) there is less of an effect on the pressure distribution than with the upstream jet alone. This is probably due to the competing effects of the jets, where the upstream jet tends to pull the flow down (towards the lower surface) while the downstream jet pulls the flow up (towards the upper surface). Furthermore, the forcing level of the combined jets is  $\hat{m} = 3\%$  (1.5% for each jet), which is insufficient to adequately reattach the flow on either surface.

The streamwise distributions of the pressure coefficient along the upper surface of the duct are presented in Figure 7b. For the baseline case, the flow is attached up to  $x/D_{AIP} \approx 1.3$ , followed by a separated region. Note that due to the small radius of curvature ( $r/D_{AIP} = 0.22$ ) of the second turn around  $x/D_{AIP}$  of 1.18 the flow is significantly accelerated, as is seen by the presence of a large suction peak. When the downstream control is activated, the magnitude of the suction peak is increased from

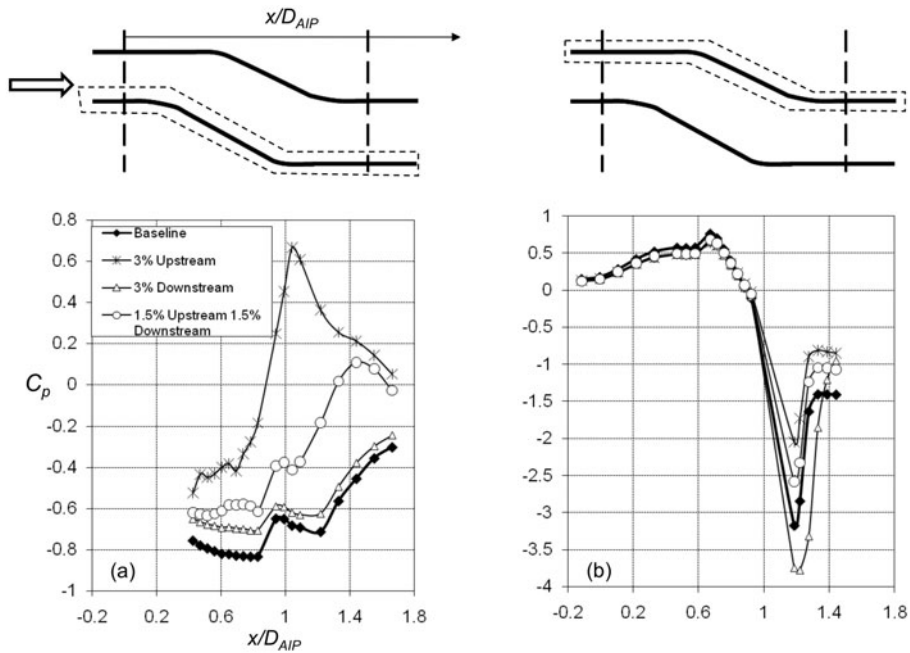


Figure 7. Pressure coefficient distributions along the duct centerline on the lower surface (a) and upper surface (b).  $M = 0.2$ ,  $C_{\mu} = 0.0316$ . The dashed lines represent the streamwise location of the inlet and the AIP.

$C_p = -3.2$  to  $-3.8$ . For this case, the blowing ratio (i.e., the jet's Mach number at its exit plane divided by the inlet Mach number) is 1.97. Note that due to the significant acceleration of the flow around the turn the local blowing ratio (i.e., the jet's Mach number divided by the local Mach number at the location of the control jet) is much smaller. From the static pressure at  $x/D_{AIP}$  of 1.18 and the total pressure, the local Mach number is 0.26 and thus the local blowing ratio is 1.5. Furthermore, activation of either the upstream jet alone or combined with the downstream jet results in negative effect on the flow.

The effect of flow control on the pressure distribution in the inlet duct was also examined at higher Mach numbers of 0.325 and 0.45. For brevity, only the Mach numbers of 0.45 with  $C_{\mu} = 0.012$  ( $\hat{m} = 3\%$ ) forcing

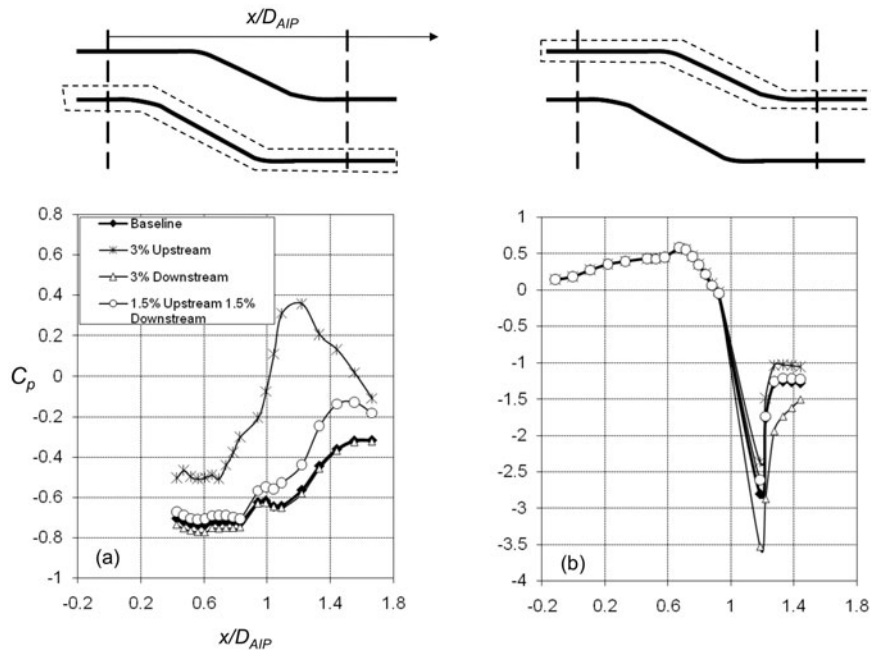


Figure 8. Pressure coefficient distributions along the duct centerline: lower surface (a) and upper surface (b).  $M = 0.45$ ,  $C_{\mu} = 0.012$ . The dashed lines represent the streamwise location of the inlet and the AIP.

case is presented in Figure 8. At this Mach number, activation of the upstream control jet results in a large peak on the lower surface while activation of the downstream jet increases the suction peak on the upper surface. However, the effect is somewhat smaller compared to that on the lower Mach number of 0.2 case. Note that the blowing ratio for  $M = 0.45$  (at a forcing level of 3%) is 1.20, compared to a blowing ratio of 1.97 for  $M = 0.2$  at the same forcing level. This may also explain why the flow control is more effective at the lower Mach number case. The effect of the blowing ratio is discussed in more detail in Section 4.4.

These results clearly show that flow control via fluidic actuation of steady jets can affect the pressure distribution along the walls of the inlet duct (and thus the flow field). While activating each jet by itself has a large effect on the pressure distribution on the wall where the control jet resides, activating both jets together results in a degradation of the performance (compared to each jet by itself). This is due to both the competing effect of the jets, as was discussed earlier, and the lower forcing level for each control jet.

As was mentioned in the introduction, the flow field associated with the inlet duct consists of secondary flow structures, which yield a highly 3-D flow field. This was examined by measuring the pressure distributions along the walls at two spanwise locations on either side of the centerline at a distance of 44.45mm (or  $z/D_{AIP} = 0.111$  and 0.809). Figure 9 presents the pressure distributions along the lower wall for  $C_{\mu} = 0.012$  ( $\dot{m} = 3\%$ ) at Mach number of 0.45. Without flow control (represented by the open symbols with solid and dash lines for the centerline and off-centerline cases, respectively) the streamwise extent of the separated region is the same, however, the pressure recovery that follows (for  $x/D_{AIP} > 0.9$ ) is larger off centerline. When flow control is applied (represented by the solid symbols) it is clear that flow control is much less effective off-centerline compared to the centerline. This is probably related to the formation of the secondary flow structures (i.e., highly 3-D distribution) while the flow control used here is two dimensional. This will be discussed in more detail in the next section.

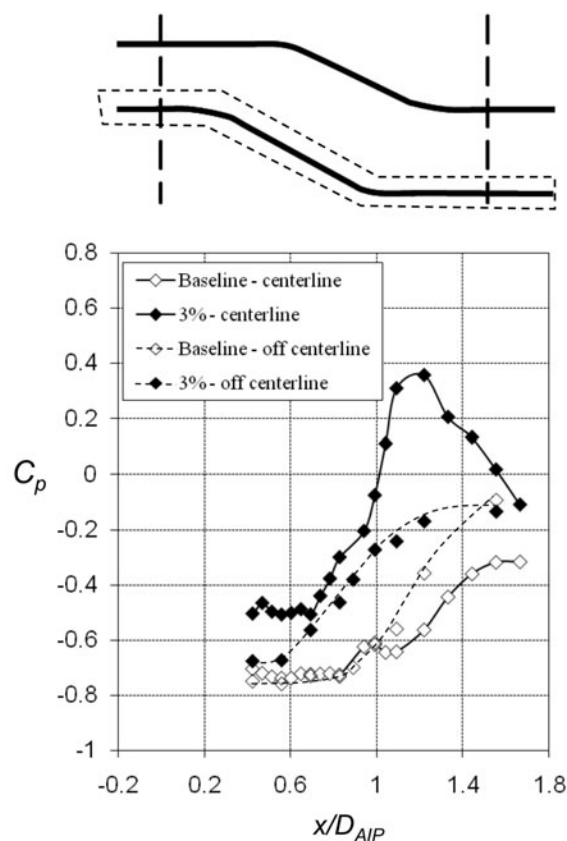


Figure 9. Pressure coefficient distributions along the duct at  $z/D_{AIP} = 0.11$  and 0.5 for  $M = 0.45$ ,  $C_{\mu} = 0.012$ .

The static pressure coefficient based on URANSS and DES predictions for the baseline flow case at the lower surface along centerline and off-centerline are presented in Figure 10. Experimental measurements (symbols) are also included to provide a comparison with the numerical results. It is

clear that the DES predictions are in much better agreement with the experimental measurements than the URANSS results obtained on both the meshes, especially at the centerline. URANSS predictions on both coarse ( $M_{\text{coarse}}$ ) and fine ( $M_{\text{fine}}$ ) meshes are relatively similar indicating that negligible improvements are gained in URANSS results due to grid refinements in regions of interest. Specifically, URANSS predicts much higher values of pressure coefficient at the centerline (for  $x/D_{AIP} > 1$ ). Indeed, the high  $C_p$  values are due to URANSS prediction of flow impingement on the lower surface which will become clearer from the pressure recovery plots shown in Figure 14.

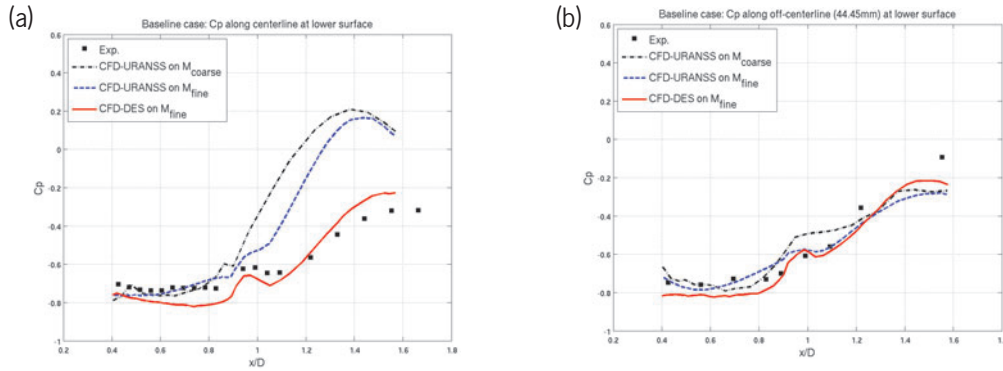


Figure 10. Comparison between experimental measurements and numerical predictions of the pressure coefficient distributions for the baseline flow case at  $M = 0.45$  on the lower wall along the duct (a) centerline and (b) off-centerline (44.45mm) at  $z/D_{AIP} = 0.11$ .

## 4.2 AIP Measurements – $h = 1\text{mm}$

As was mentioned in the introduction section, in a well designed inlet the flow must be decelerated whilst achieving as uniform a flow as possible at the compressor face with minimum stagnation pressure loss. Therefore, the pressure recovery,  $PR$ , distributions at the AIP were measured and are presented in this section. The pressure recovery is defined as:

$$PR = \frac{\text{Avg}(P_1 : P_{45})}{P_o} \quad (5)$$

Due to symmetry, 45 measurement locations were measured (see Figure 4 above), and were used to calculate the pressure recovery distributions presented in Figures 11 to 14. Figure 11 presents the pressure recovery distributions for  $M = 0.2$  for the baseline case (Figure 11a) and actuated cases with  $C_{\mu} = 0.0316$  ( $\dot{m} = 3\%$ ) using the downstream control jet (Figure 11b), the upstream control jet (Figure 11c), and both jets operating together (Figure 11d). Without flow control, there is a total pressure loss at the upper portion of the AIP (for  $Y/D_{AIP} > 0.85$ ) due to the separation around the second turn on the upper wall (as was also suggested by the pressure distribution along the upper wall, Figure 8b above). In addition, there is a large region of pressure loss on the lower portion of the AIP, which is due to the separation around the upstream turn on the lower surface. Furthermore, the pressure loss is not uniform in the spanwise direction due to the formation of the secondary structures, as discussed with respect to Figure 9. Note that the average pressure recovery for this case is 0.985. When the downstream jet is activated, there is a deteriorating effect on the pressure recovery in the upper left corner. On the other hand, when the upstream jet is turned on there is a significant improvement in the lower part of the AIP, due to the reattachment of the flow along the centerline. However, there is a region on the left bottom corner of the AIP where there is an increase in pressure loss. This might be due to the fact that the flow control is 2-D and since the flow is 3-D, the secondary vortices are pushed to the corner. Another plausible explanation is that the control jet slit extends 101.6mm (out of 114.3mm of the span), which means that there is no control jet between  $0 \leq z/D_{AIP} \leq 0.055$  and  $0.945 \leq z/D_{AIP} \leq 1$ . Activation of both jets together shows improved performance with increased reattachment on the lower surface and minimal effect on the upper surface. The average  $PR$  for the upstream is 0.989 which is an improvement over the baseline, while the downstream jet is 0.982, which is worse than the baseline. Another way to

show the effectiveness of each jet is to average the pressure recovery only with half of the AIP (bottom half for the upstream jet case, and upper half for the downstream jet). In these cases, activation of the upstream jet results in a pressure recovery of 0.990 (compared to 0.985 of the baseline), while the pressure recovery for the downstream jet case is 0.986 (compared to 0.982).

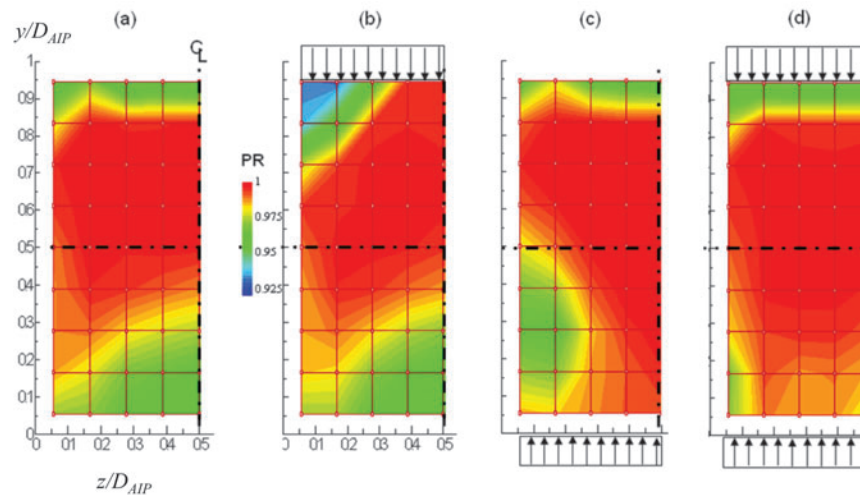


Figure 11. Pressure recovery distributions at the AIP for  $M = 0.2$ ; baseline (a) and actuated cases with  $C_\mu = 0.0316$ : downstream jet (b), upstream jet (c), and both jets together (d).

The effect of the Mach number on the pressure recovery is presented in Figures 12a, b and c at  $z/D_{AIP} = 0.11, 0.28$  and  $0.5$ , respectively. Clearly, as the Mach number increases the pressure loss increases on both top and bottom portions of the AIP. This suggests that the flow control may be less effective (at the same forcing level).

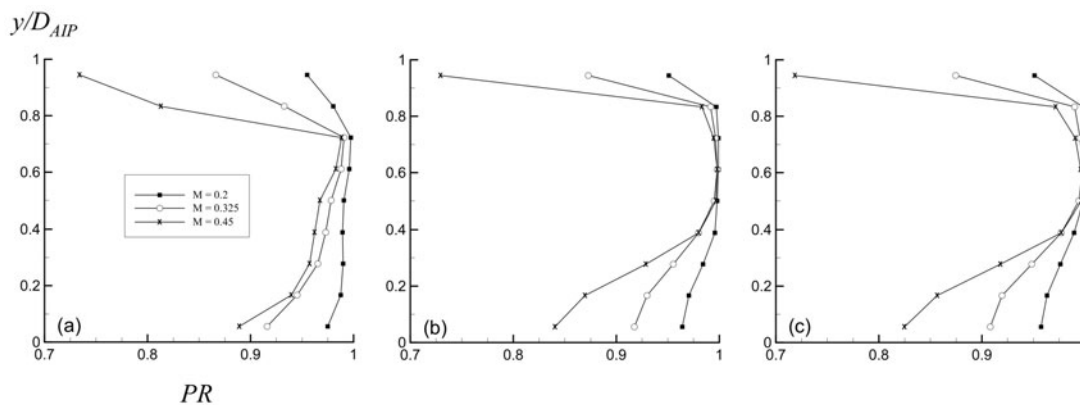


Figure 12. Effect of the Mach number on the pressure recovery.  $z/D_{AIP} =$  (a) 0.11, (b) 0.28 and (c) 0.5.

The effect of flow control on the AIP pressure recovery was also examined at a higher Mach number of 0.45 and is presented in Figure 13 for  $C_\mu = 0.012$  ( $\hat{m} = 3\%$ ). As the Mach number increases the pressure loss increases (note the contour levels on the plots). The pressure recovery for the baseline case at Mach number of 0.45 is 0.925 compared to 0.985 at  $M = 0.2$ . As was shown in the static pressure distributions along the walls, the effect of flow control is smaller (for all control cases) compared to the  $M = 0.2$  case. Increasing the blowing ratio (for the same forcing level) may be the next logical step. This will be achieved by reducing the width of the slit, which will result in a higher jet Mach number (this is addressed in Section 4.4).

The pressure recovery values obtained from the simulations at the AIP plane along the centerline and off-centerline locations are shown in Figure 14a. Numerical results for the baseline flow case at  $M = 0.45$  are shown along with the experimental measurements. Similar to the predictions of static pressure

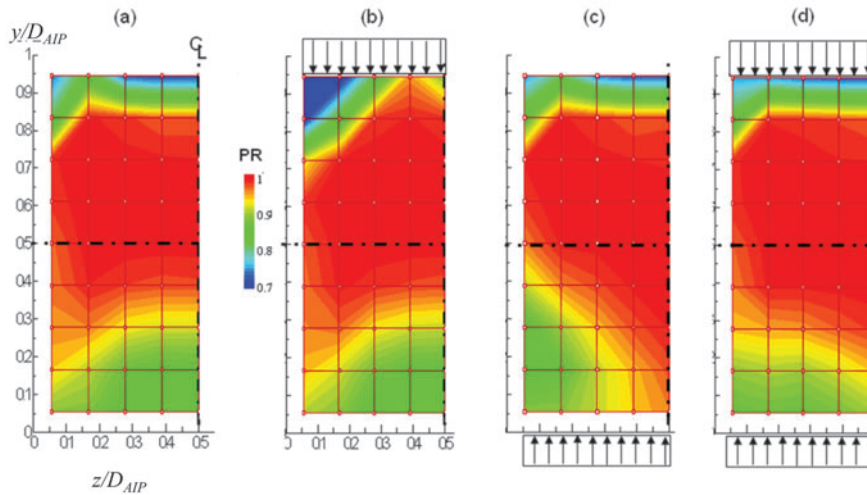


Figure 13. Pressure recovery distributions at the AIP for  $M = 0.45$ ; baseline (a) and actuated cases with  $C_{\mu} = 0.012$ : downstream jet (b), upstream jet (c), and both jets together (d).

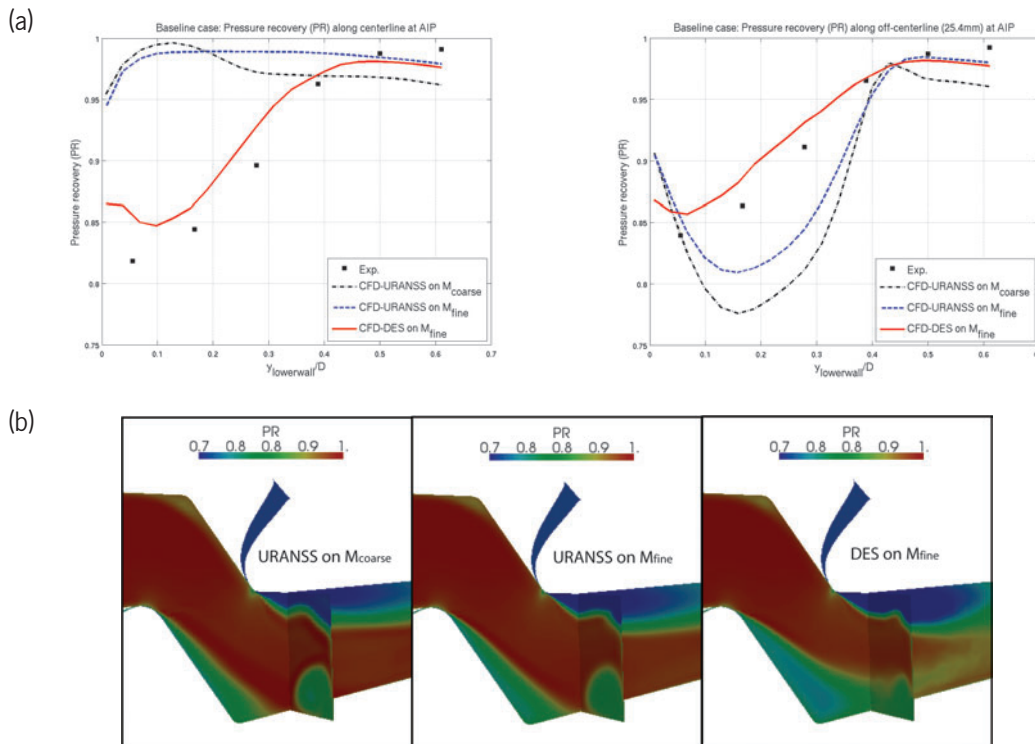


Figure 14. (a) Comparison of the pressure recovery for the baseline flow case at the AIP between the experiments and two simulation models: URANSS and DES, and (b) Comparison of pressure recovery field obtained from three numerical simulations; URANSS on  $M_{coarse}$ , URANSS on  $M_{fine}$  and DES on  $M_{fine}$

coefficient, the pressure recovery values obtained through DES are in much better agreement with the experimental measurements than those of the URANSS. As noted before, URANSS predicts much higher pressure values at the centerline-wall. Figure 14b provides further evidence, where pressure recovery fields obtained from URANSS and DES are shown at the AIP plane and the vertical center-plane. Large vortices at the lower corners are predicted by URANSS (on both the meshes) whereas DES appears to either breakup or otherwise disrupt the formation of these large corner vortices. These large corner vortices in the case of URANSS predictions cause the flow to impinge on the lower surface at the centerline resulting in a shorter separation and leading to higher centerline values of pressure

recovery, and also the pressure coefficient, which is in disagreement with the experimental measurements. Clearly a higher fidelity turbulence model such as DES is required to predict flow of this complexity. Further cycles of mesh refinements are underway to strengthen the current observations and establish grid independence of the DES result.

### 4.3 AIP Measurements – Effect of Actuation Frequency

In this section the effect of the actuation frequency was investigated. For ease of the analysis only the upstream jet was activated and the pressure recovery at the AIP was calculated for the lower left portion of the AIP (25 data points were used).

Figure 15 presents the pressure recovery distributions at the bottom quadrant for  $M = 0.45$  and  $h = 1\text{mm}$  for the baseline case (Figure 15a) and actuated cases at  $C_\mu = 0.002$  using steady blowing (Figure 15b), and unsteady blowing with actuation frequencies of  $f_{act} = 350\text{Hz}$  (Figure 15c),  $800\text{Hz}$  (Figure 15d), and  $1200\text{Hz}$  (Figure 15e). Without flow control, there is a large region of pressure loss on the lower portion of the AIP due to the separation around the first (upstream) turn on the lower surface. Furthermore, the pressure loss is not uniform in the spanwise direction due to the formation of the secondary structures, as discussed in Figure 9.

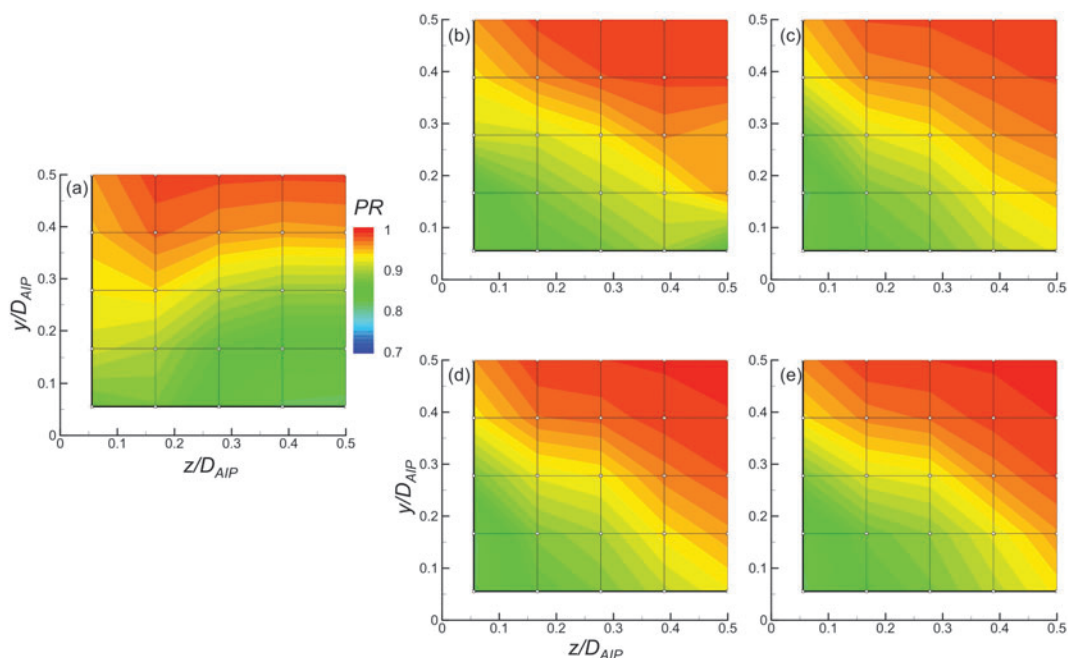


Figure 15. Pressure recovery distribution at the bottom quadrant of the AIP. Baseline (a), and forcing with  $C_\mu = 0.002$ : steady blowing (b),  $f_{act} = 350\text{Hz}$  (c),  $800\text{Hz}$  (d), and  $1200\text{Hz}$  (e).  $M = 0.45$ ,  $h = 1\text{mm}$ .

When the control jet is activated in a steady mode (Figure 15b) there is some improvement of the pressure recovery, especially near the centerline. When an unsteady jet is used there is a significant improvement in the lower part of the AIP, due to the reattachment of the flow along the centerline. However, there is a region on the left bottom corner of the AIP where there is an increase in pressure loss. The effect of unsteady blowing seems to be larger than the steady blowing, regardless of the actuation frequency used. Note that the shedding frequency of the separated shear layer is  $\sim 370\text{Hz}$  and thus the unsteady forcing takes advantage of the naturally unstable modes in the flow to improve the flow control efficiency.

### 4.4 AIP Measurements – Effect of Blowing Ratio

Next, the effect of the blowing ratio (for a fixed momentum coefficient) was explored. As was shown in literature, the momentum coefficient is not necessarily a unique parameter to quantify the flow control, and the blowing ratio must also be considered. In order to show the effect of the blowing ratio, the control jet width was changed to  $0.5\text{mm}$  such that when the momentum coefficient of this case is the same as for the larger slit case the blowing ratio is larger (for a  $C_\mu = 0.002$  the blowing ratio  $C_b = 1.31$  and  $0.356$  for  $h = 0.5\text{mm}$  and  $1\text{mm}$ , respectively).

Figures 16a-d present the pressure recovery for the baseline cases (Figure 16a for  $h = 1\text{mm}$ , and Figure 16b for  $h = 0.5\text{mm}$ ) and the forcing cases with steady blowing having a momentum coefficient of  $C_\mu = 0.002$  (Figures 16c and d for  $h = 1\text{mm}$ , and  $0.5\text{mm}$ , respectively). For both slit widths the distribution of the pressure recovery of the baseline case is very similar, suggesting that the presence of the slit does not have a significant effect on the AIP. The effect of the slit width (or the blowing ratio) on the control effectiveness is clearly visible by comparing Figures 16c and d. The effect of the lower blowing ratio (Figure 16c) was discussed in the previous section and is shown here for reference. When the blowing ratio is increased to 1.31 (for the same  $C_\mu$ ), the effectiveness of the flow control is more pronounced, especially along the centerline, where the flow is almost fully attached. Based on this results, it was decided that for the remainder of the paper to concentrate on flow control where the slit width is  $0.5\text{mm}$ , which results in a larger blowing ratio for a given momentum coefficient.

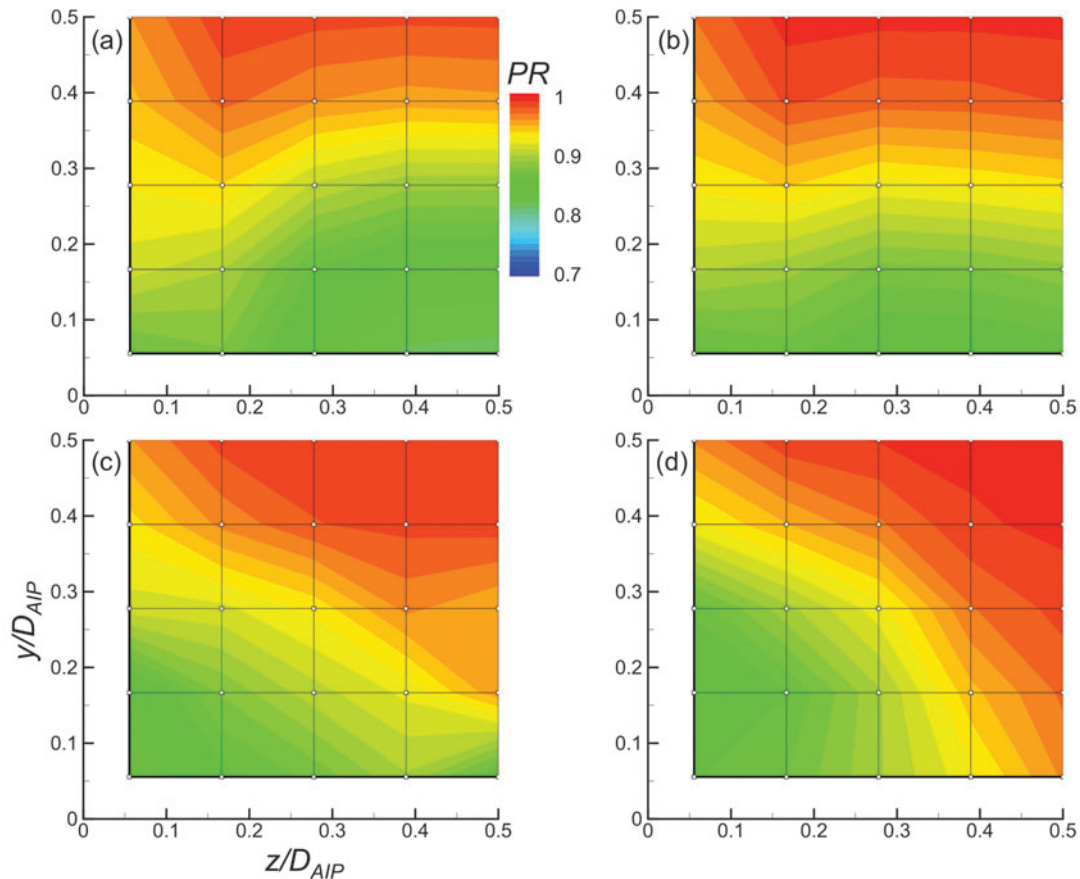


Figure 16. The effect of the blowing ratio on the pressure recovery distribution at the bottom quadrant of the AIP. Baseline (a, b), and steady blowing with  $C_\mu = 0.002$  (c, d).  $h = 1\text{mm}$  (a, c), and  $0.5\text{mm}$  (b, d).

#### 4.5 PIV Measurements

In order to explore the interaction between the control jets and the main flow, PIV measurements were conducted in the vicinity of the upstream control jet (see schematics in Figure 5b). Figures 17a-i present the velocity vector fields colored by the total velocity magnitude, where Figures 17a, d, g show the baseline cases, Figures 17b, e, h show the actuated cases with steady blowing at  $C_\mu = 0.002$ , while Figures c, f, i represent the actuation cases with  $C_\mu = 0.008$ . The velocity fields were measured at three measurement planes:  $z/D_{AIP} = 0.5$  (along the centerline, Figures 17a-c), and  $z/D_{AIP} = 0.367$  and  $0.238$  (Figures 17d-f and 17g-i, respectively). Without flow control, the flow separates immediately downstream of the turn and stays separated throughout the remainder of the measurement domain. Note that the cross-stream extent of the separated region decreases as the distance from the centerline increases, which is in agreement with Figures 9 (wall static pressure) and 15a (AIP). When flow control is applied with  $C_\mu = 0.002$  the severity of the separation is reduced. As the momentum coefficient is

increased to  $C_\mu = 0.008$  the flow is accelerated around the turn and it is completely reattached along the centerline (Figure 17c); however, the effectiveness of the flow control off centerline is significantly reduced. Furthermore, at  $z/D_{AIP} = 0.238$  flow control yields a more severe separation, which extends to about a third of the duct height. These results are in full agreement with the data collected at the AIP (Figures 15b-e). The PIV data clearly show that by directing the control jet tangential to the surface the flow control takes advantage of the Coanda effect.

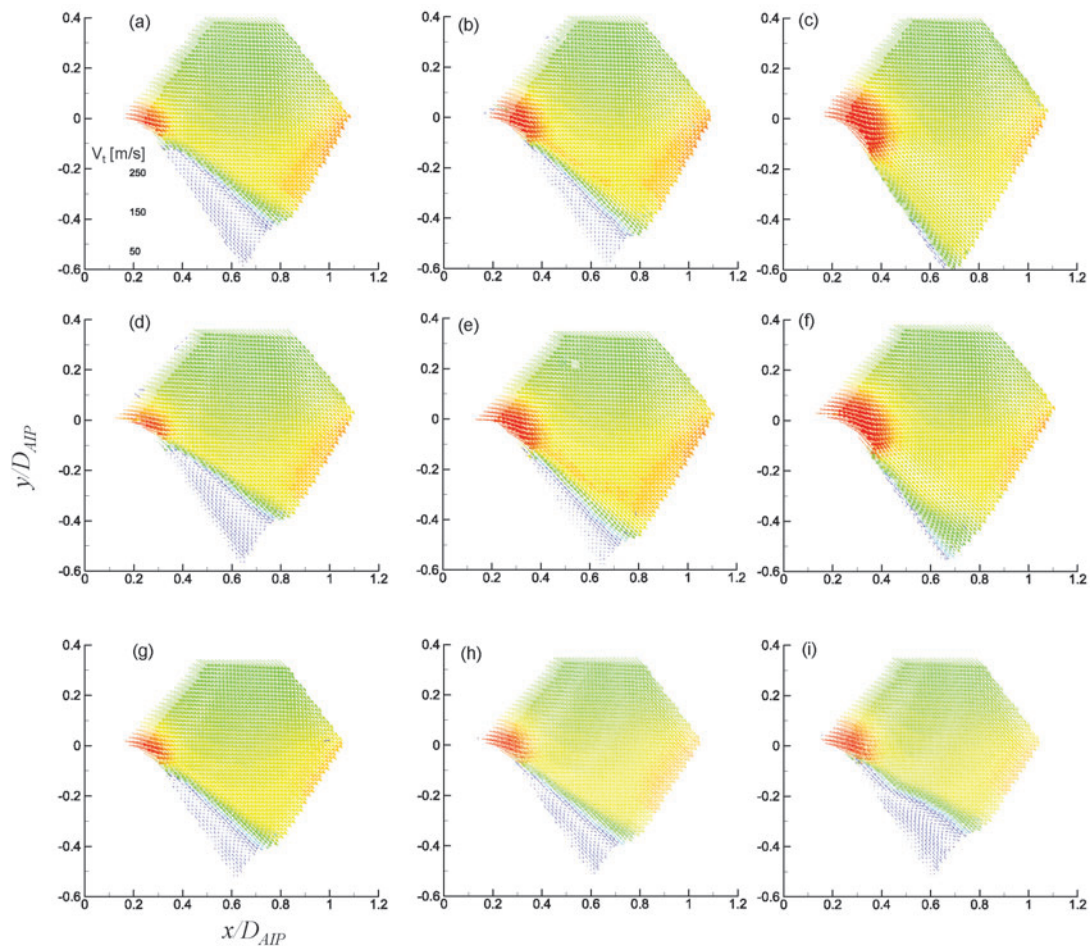


Figure 17. Velocity vector field of the baseline flow (a, d, g), and actuated cases with  $C_\mu = 0.002$  (b, e, h), and  $0.008$  (c, f, i) at  $z/D_{AIP} = 0.5$  (a-c),  $0.367$  (d-f), and  $0.238$  (g-i).  $M = 0.45$ ,  $h = 0.5\text{mm}$ .

#### 4.6 Unsteady Pressure

The effect of flow control on the unsteady pressure along the lower wall and at the AIP was also investigated. First, the time traces of the total pressure along the centerline were measured and compared to the instantaneous pressure in the actuator cavity. Figure 18 presents the instantaneous pressure data for the baseline (i.e., no flow control, Figure 18a), steady blowing (with  $C_\mu = 0.002$  and  $0.008$ , Figures 18b and c, respectively), and unsteady blowing with  $f_{act} = 350\text{Hz}$  (with  $C_\mu = 0.002$  and  $0.008$ , Figures 18d and e, respectively). Similar results were obtained for actuation frequency of  $800\text{Hz}$ , and  $1200\text{Hz}$ , and are not shown here for brevity. Without flow control the wall pressure is below atmospheric and fluctuates at a frequency of about  $370\text{Hz}$ , which corresponds to the shedding frequency of the separated mixing layer due to the upstream bend. At location 3 the pressure increases slightly; however, its RMS value increases compared to locations 1 and 2. Note also the sub-atmospheric pressure at the actuator cavity due to the cross-flow over the actuator slit. When steady blowing is used there is a significant increase in the wall pressure and an attenuation of the fluctuations at the shedding frequency due to reduction of the severity of the separation (for  $C_\mu = 0.002$ , Figure 18b)

or the complete reattachment of the flow (for  $C_\mu = 0.008$ , Figure 18c) along the centerline. When an unsteady jet is used (with  $f_{act} = 350\text{Hz}$ ) the results are similar to the steady blowing; however, the presence of the fluctuations at the forcing frequency is clearly visible, especially for the lower momentum coefficient case (Figure 18d). This is not surprising since the actuation frequency corresponds with the shedding frequency of the separated flow and thus low momentum coefficient amplifies the coherent structures, while high momentum coefficient results in flow reattachments which results in an attenuation of these structures. Furthermore, the high actuation level most likely yields a bypass to highly non-linear behavior. Moreover, the averaged pressure at the actuator cavity is significantly lower than the steady blowing case, suggesting that unsteady blowing is more efficient.

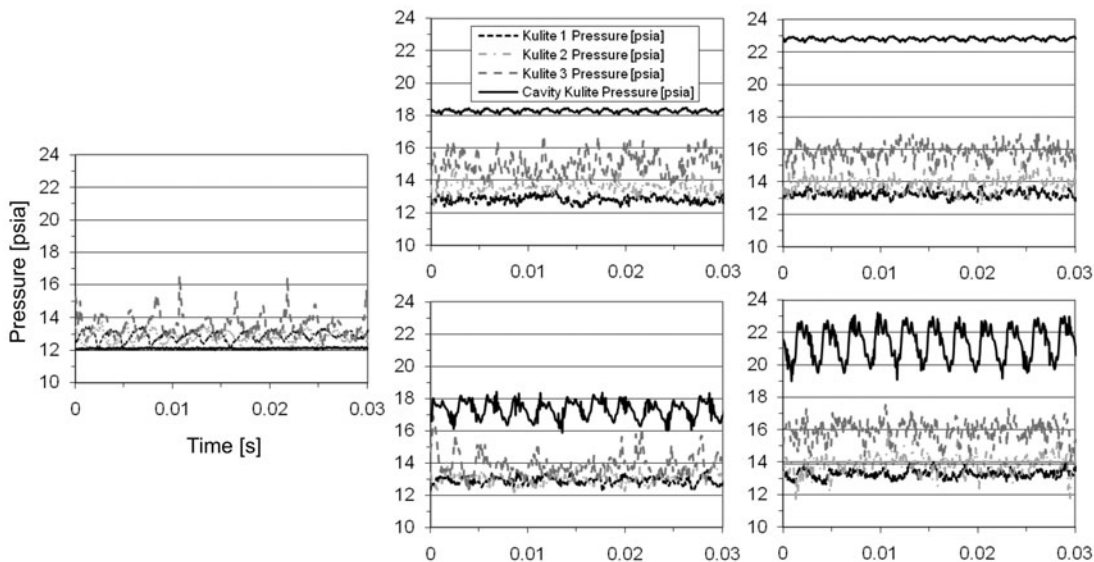


Figure 18. Instantaneous unsteady surface pressure on the lower wall of the duct along its centerline, as well as the unsteady pressure in the actuator resonance cavity. Baseline (a), steady blowing with  $C_\mu = 0.002$  (b) and  $0.008$  (c), and unsteady blowing at  $f_{act} = 350\text{Hz}$  with  $C_\mu = 0.002$  (d) and  $0.008$  (e).

As was shown above, the distribution of the pressure recovery at the AIP is three-dimensional, especially when a high momentum control jet is activated. Furthermore, the steady surface pressure data presented in Figure 9 clearly shows the spanwise non-uniformity, which is present for both the baseline and forced cases, and is much more pronounced as the downstream distance increases. This was also examined by measuring the instantaneous wall pressure at locations 1, 4, and 5 (see schematics in Figure 5, where the streamwise location is the same but the sensors are placed on and off the centerline) and is presented in Figures 19a-e. Without flow control (Figure 19a) the flow seems to be two dimensional where both the phase and the amplitude of the wall pressures are similar across the span (this is in agreement with the data presented in Figure 9 for the steady pressure). Note that three-dimensionalities are visible only farther downstream for  $x/D_{in} > 1$ . When flow control is applied at low momentum coefficient for both steady and unsteady blowing (Figures 19b and d, respectively) the flow just downstream of the upstream bend is two dimensional. However, three dimensionalities are clearly visible when high momentum coefficient is used (Figures 19c and e) where the pressure at the centerline is higher than the sides, which agrees with the steady pressure data (Figure 9), the AIP data (Figures 15 and 16), and the PIV data (Figure 17).

In addition to unsteady wall pressure, the unsteady total pressure at the AIP ( $y/D_{AIP} = 0.306$  and  $z/D_{in} = 0.5$ ) was measured, and is presented Figures 20a-e superimposed with the unsteady pressure in the actuator cavity. Without flow control (Figure 20a) the average pressure at the AIP is  $\sim 14\text{psia}$  and with an RMS of  $\sim 0.48\text{psia}$ . When flow control is applied the average total pressure at the AIP increases for all cases (the larger momentum coefficient results in a larger increase in the total pressure). Note, however, that the RMS level for the steady blowing is lower than the unsteady blowing especially for the lower momentum coefficient case (Figures 20b and d).

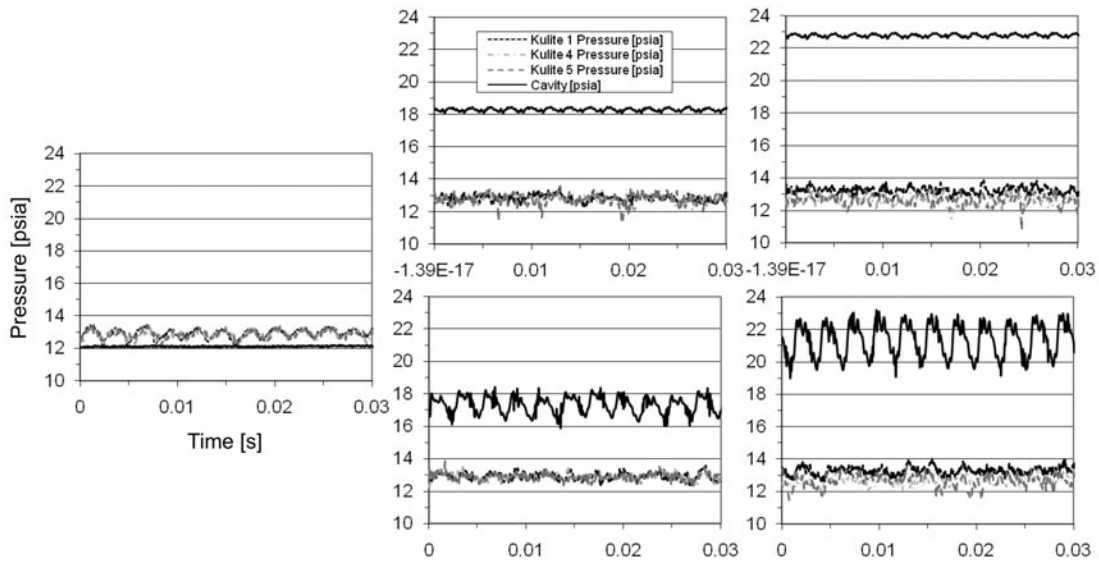


Figure 19. Instantaneous unsteady surface pressure on the lower wall of the duct at  $x/D_{in} = 0.47$  and  $z/D_{AIP} = 0.83$ , and  $1.12$ , as well as the unsteady pressure in the actuator resonance cavity. Baseline (a), steady blowing with  $C_{\mu} = 0.002$  (b) and  $0.008$  (c), and unsteady blowing at  $f_{act} = 350\text{Hz}$  with  $C_{\mu} = 0.002$  (d) and  $0.008$  (e).

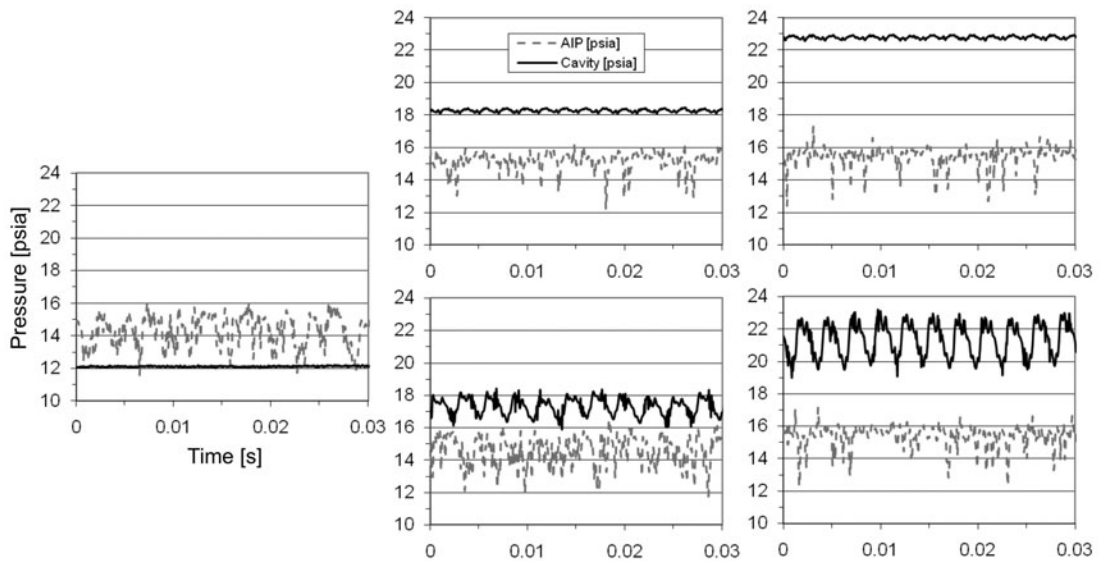


Figure 20. Instantaneous unsteady surface pressure at the AIP ( $y/D_{AIP} = 0.306$ ), as well as the unsteady pressure in the actuator resonance cavity. Baseline (a), steady blowing with  $C_{\mu} = 0.002$  (b) and  $0.008$  (c), and unsteady blowing at  $f_{act} = 350\text{Hz}$  with  $C_{\mu} = 0.002$  (d) and  $0.008$  (e).

Finally, the power spectra of the total pressure at the AIP were calculated from the unsteady pressure data and are presented in Figures 21a and b for  $C_{\mu} = 0.002$ , and  $0.008$ , respectively. Three cases are presented in each figure: the baseline case, steady blowing, and unsteady blowing. The baseline case (grey line) exhibits a large peak at  $\sim 370\text{Hz}$ , corresponding to the shedding frequency of the separated flow. In addition, there are two smaller peaks at  $600\text{Hz}$  (which may correspond to the shedding frequency of the flow from the upper bend of the duct) and at  $\sim 740\text{Hz}$ , which is the first harmonic of the shedding frequency. Also notice a small peak at  $60\text{Hz}$ , which is due to electronic noise. When steady blowing is applied at low momentum coefficient (black line, Figure 21a) the magnitude of the peaks is significantly reduced. As the momentum coefficient is increased to  $0.008$ , there is a significant reduction in the turbulent kinetic energy for frequencies lower than  $600\text{Hz}$ . The results for the unsteady

blowing case are similar, except for the presence of peaks at the fundamental actuation frequency and its higher harmonics (for the low momentum coefficient case, Figure 21a), and a small peak at the first harmonic (for the high momentum coefficient case, Figure 21b).

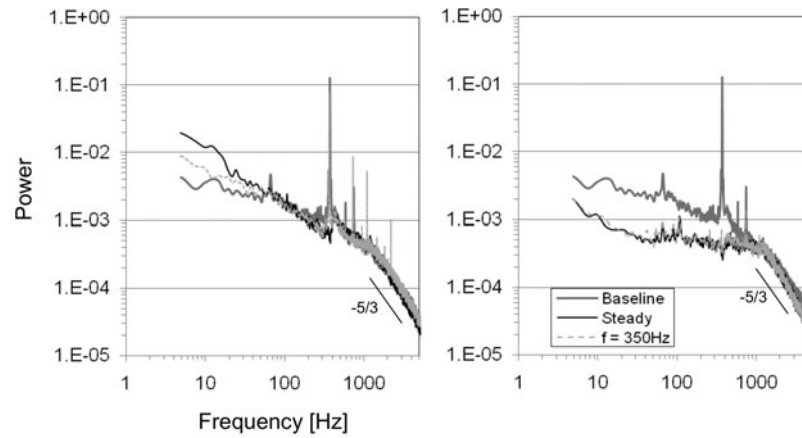


Figure 21. Power spectra at the AIP ( $y/D_{AIP} = 0.306$ ).  $C_{\mu} = 0.002$  (a) and  $0.008$  (b).

## 5. SUMMARY AND CONCLUSIONS

The effectiveness of active flow control to improve the performance of a very short inlet duct was investigated experimentally in a custom made facility and the results were compared to numerical simulations. The length to exit diameter ratio,  $L/D$ , of the duct was 1.5 and it was tested through a range of inlet Mach numbers from 0.2 to 0.45. A pair of control jets was placed in streamwise locations where flow was expected to separate (one on the upper wall and one on the lower wall).

The results show that flow control via steady or unsteady jet actuation can alter the pressure distribution along the walls of the inlet duct (and thus the flow field inside the duct). While activating each jet by itself has a large effect on the pressure distribution on the wall where the control jet resides, activating both jets together results in a degradation of the performance (compared to that of each jet by itself). This is due to: (1) the competing effect of the jets (the upstream jet pulls the flow down while the downstream jet pulls the flow up), and (2) the lower forcing level (and lower blowing ratio) for each control jet.

The results show that in order to characterize flow control one needs to provide both the control jet's momentum coefficient as well as its blowing ratio. It was shown that for a fixed momentum coefficient increasing the blowing ratio results in a larger effect of the flow. In addition, since the flow field associated with the inlet duct consists of secondary flow structures, which yield a highly 3-D flow field, the effect of 2-D actuation is somewhat limited. When flow control is applied, it is much less effective off-centerline compared to the centerline, suggesting that spanwise distribution of jets is needed (instead of one long slit that covers the entire span).

The effect of unsteady blowing is larger than steady blowing at low momentum coefficient. However, as the momentum coefficient is increased to a level that yields flow reattachment (along the centerline) there is hardly any difference between the two actuation techniques. This was also explored by measuring the unsteady total pressure along and off the centerline, as well as at the AIP. Using steady blowing there is a significant increase in the wall pressure and an attenuation of the fluctuations at the shedding frequency due to reduction of the severity of the separation (for low  $C_{\mu}$ ) or the complete reattachment of the flow (for the higher  $C_{\mu}$  case) along the centerline. When the unsteady control jet is used the results are similar to the steady blowing; however, the presence of the fluctuations at the forcing frequency is clearly visible, especially for the lower momentum coefficient case. More importantly, the averaged pressure at the actuator cavity is significantly lower when unsteady blowing is activated, compared to steady blowing, suggesting that unsteady blowing is more efficient.

The numerical simulations presented in the paper were obtained for the baseline flow case at  $M = 0.45$  using two variants of the Spalart-Allmaras model including URANSS and DES. Numerical results (based on URANSS and DES) were compared with the experimental measurements of static and total pressure. DES predictions provided good agreement with the experimental measurements whereas the URANSS predictions were poor. The failure of URANSS appears to be linked to its prediction of very

strong and stable corner vortices which impinge flow near the centerline in lower-wall region resulting in high pressure values which are in disagreement with the experimental measurements. The mesh was adapted to improve the resolution in the separated flow regions by a factor of two. The URANSS predictions showed negligible improvement from the grid refinement confirming that the deficiency was attributable to the turbulence model and not the discretization. It was shown that a higher fidelity turbulence model such as DES is required to predict this complex flow with adverse pressure gradients and flow separation. Work is underway to simulate flow control cases similar to the ones considered in the experiments and comparison for those cases will be considered in future.

## ACKNOWLEDGEMENT

This work was mainly supported by the Northrop Grumman Corporation (monitored by Ms. Florine Cannelle) and in part by the Center for Automation Technologies and Systems (CATS) under a block grant from the New York State Foundation for Science, Technology and Innovation (NYSTAR). The support of work done by Dr. Onkar Sahni and Prof. Kenneth E. Jansen was provided by NSF under grant OCI-0749152. Computing resources were provided in part by the NSF through TeraGrid resources at Texas Advanced Computing Center (Ranger and Spur systems were used) and by Rensselaer's Computational Center for Nanotechnology Innovations which was funded by the State of New York, IBM and Rensselaer Polytechnic Institute. The numerical results presented in this article made use of the linear algebra library provided by ACUSIM Software Inc. We would also like to acknowledge that we made use of ParaView software provided by Kitware Inc. for visualization of simulation data. The help of Mr. Joseph Vasile, Mr. Joshua Wood, and Mr. Brian Belley in designing and assembling the experimental facility are greatly appreciated. Help from Mr. Ben Wright is also appreciated in carrying out some of the simulations and post-processing of the simulation data.

## REFERENCES

- Ahuja, K.H. and Burrin, R.H., 1984, "Control of flow separation by sound", *AIAA/NASA 9<sup>th</sup> Aeroacoustics Conference*, Williamsburg, Virginia, AIAA-84-2298.
- Allan, B.G., Yao, C.S., Lin, J.C., "Numerical Simulations of Vortex Generator Vanes and Jets on a Flat Plate", *AIAA 2002-3160*.
- Amitay, M., Pitt, D. and Glezer, A., "Separation Control In Duct Flows", *Journal of Aircraft* Vol. 39, No. 4, pp. 616-620, 2002.
- Amitay, M. and Glezer, A., 1999, "Aerodynamic Flow Control of a Thick Airfoil using the Synthetic Jet Actuators", *Proceedings of the 3rd ASME/JSME Joint Fluids Engineering Conference*, San Francisco, California.
- Amitay, M. and Glezer, A., 2002, "Role of Actuation Frequency in Controlled Flow Reattachment over a Stalled Airfoil", *AIAA Journal*, Vol. 40, No. 2, pp. 209-216.
- Amitay, M., Smith, D.R., Kibens, V., Parekh, D.E., and Glezer, A., "Modification of the Aerodynamics Characteristics of an Unconventional Airfoil using Synthetic Jet Actuators", *AIAA Journal* 2001; **39**: 361-370.
- Debiasi, M., Herberg, M. R., Yan, Z., Dhanabalan, S. S., Tsai, H. M., 2008, "Control of Flow Separation in S-ducts via Flow Injection and Suction", *46th AIAA Aerospace Sciences Meeting and Exhibit, 7 – 10 January 2008*, Reno, Nevada, AIAA 2008-74.
- Garimella, R.V. and Shephard, M.S., 2000, "Boundary Layer Mesh Generation for Viscous Flow Simulations", *International Journal of Numerical Methods in Engineering*, Vol. 49, pp. 193-218.
- Glezer, A. and Amitay, M., "Synthetic Jets", *Annual Review of Fluid Mechanics*, 2002, **34**.
- Hamstra, J. W., Miller, D.N., Truax, P.P., Anderson, B.A. and Wendt, B.J., "Active Inlet Flow Control Technology Demonstration", *The Aeronautical Journal*, Oct. 2000, pp. 473.
- Ho., C.-M. and Huerre, P., 1984, "Perturbed Free Shear Layers", *Annual Review of Fluid Mechanics*, Vol. 16, pp. 365-424.
- Jansen, K.E., 1999, "A Stabilized Finite Element Method for Computing Turbulence," *Computer Methods in Applied Mechanics and Engineering*, 174, 299-317.
- Jansen, K.E., Whiting, C.H., and Hulbert, G.M., 1999, "A Generalized Alpha Method For Integrating The Navier-Stokes Equations With A Stabilized Finite Element Method," *Computer Methods in Applied Mechanics and Engineering*; 190, 305-319.

- Luers, A.S., "Flow Control Techniques in a Serpentine Inlet: An Enabling Technology to Increase the Military Viability of Unmanned Air Vehicles", M.S. thesis, Aeronautics and Astronautics Dept., Massachusetts Institute of Technology, Cambridge, MA, June 2003.
- Neuberger, D. and Wygnanski, I., "The Use of a Vibrating Ribbon to Delay Separation on Two Dimensional Airfoils", *Proceedings of Air Force Academy Workshop in Unsteady Separated Flow 1987*. Colorado Springs, CO.
- Oster, D. and Wygnanski, I.J., 1982, "The Forced Mixing Layer Between Parallel Streams", *J. Fluid Mech.*, 123, pp. 91-130.
- Panitz, T. and Wasan, D.T., "Flow Attachment to Solid Surfaces: The Coanda Effect", *American Institute for Chemical Engineers*, Vol. 18, No. 1, January 1972, pp. 51.
- Pirzadeh, S., 1994, "Unstructured Viscous Grid Generation by the Advancing-Layers Method", *AIAA Journal*, Vol. 32, pp. 1735-1737.
- Rabe Scribbsen, A., Ng, W., and Burdisso, R., 2006, "Effectiveness of a Serpentine Inlet Duct Flow Control Technique at Design and Off-Design Simulated Flight Conditions", *Journal of Turbomachinery*, Vol. 128, pp. 332-339.
- Saad, Y., and Schultz, M.H., 1986, "A Generalized Minimal Residual Algorithm for Solving Nonsymmetric Linear Systems", *SIAM Journal on Scientific and Statistical Computing*, Vol. 7, pp. 856-869.
- Sahni, O., Carothers, C.D., Shephard, M.S. and Jansen, K.E., "Strong Scaling Analysis of a Parallel, Unstructured, Implicit Solver and the Influence of the Operating System Interference", *Scientific Programming*, In Press.
- Sahni, O., Jansen, K.E., Shephard, M.S., Taylor C.A. and Beall, M.W., 2008, "Adaptive Boundary Layer Meshing for Viscous Flow Simulations", *Engineering with Computers*, 24(3), 267-285.
- Seifert, A., Darabi, A., and Wygnanski, I., 1996, "Delay of Airfoil Stall by Periodic Excitation", *Journal of Aircraft*, 33(4), 691-698.
- Seifert, A., Bachar, T., Koss, D., Shephelovich, M. and I. Wygnanski, I., 1993, "Oscillatory Blowing: A Tool to Delay Boundary-Layer Separation", *AIAA J.* 31(11), 2052-2060.
- Shephard, M.S, Jansen, K.E., Sahni, O. and Diachin, L.A., 2007, "Parallel Adaptive Simulations on Unstructured Meshes", *Journal of Physics: Conference Series*, 78, 012053.
- Spalart, P.R. and Allmaras, S.R., 1992, "A One-Equation Turbulence Model for Aerodynamic Flows", *AIAA Paper 92-439*.
- Spalart, P.R., Jou, W.H., Stretlets, M. and Allmaras, S.R., 1997, "Comments on the Feasibility of LES for Wings and on a Hybrid RANSS/LES Approach", *Advances in DNS/LES*, Greyden Press, Columbus, OH, 137—147.
- Tournier, S.E., Paduano, J.D. and Pagan, D., 2006, "Flow Control in a Transonic Inlet", *36th AIAA Fluid Dynamics Conference and Exhibit*, 5 – 8 June 2006, San Francisco, California, AIAA 2006-3883.
- Wygnanski, I., 2000, "Some Observations Affecting the Control of Separation by Periodic Excitation", *AIAA paper 2314-2000*.